First publ. in: Applied Physics / A, Materials Science and Processing, 74 (2002), pp. 747-753

E. GOERING[1,✉]
M. JUSTEN[1]
J. GEISSLER[1]
U. RÜDIGER[2]
M. RABE[2]
G. GÜNTHERODT[2]
G. SCHÜTZ[1]

Magnetic anisotropy of textured CrO_2 thin films investigated by X-ray magnetic circular dichroism

[1] Max-Plank-Institut für Metallforschung, Heisenbergstraße 1, 70569 Stuttgart, Germany
[2] Physikalisches Institut, Rheinisch-Westfälische Technische Hochschule Aachen, 52056 Aachen, Germany

Received: 8 January 2002/Accepted: 8 January 2002
Published online: 26 March 2002

ABSTRACT Highly *a*-axis-textured CrO_2 films have been deposited on Al_2O_3 (0001) substrates by chemical vapor deposition. CrO_2 has been found to have highly *a*-axis (010)-oriented columnar growth on a Cr_2O_3 (0001) initial layer. The six-fold surface symmetry of the Cr_2O_3 initial layer leads to three equivalent in-plane orientations of the *a*-axis-oriented CrO_2 unit cell. We report Cr $L_{2,3}$ X-ray magnetic circular dichroism data along the surface normal and at 60° off-normal sample orientation. For a 60° sample alignment, a strong increase of the projected orbital moment could be observed for unoccupied majority t_{2g} states using moment analysis. Therefore, the *c* axis is identified as the intrinsic magnetic easy axis of CrO_2. In addition, a small spin moment and a very strong magnetic dipole term T_z have been found.

PACS 75.30.Cr; 75.30.Gw; 78.20.Lj; 78.70.Dm; 78.20.Bk

1 Introduction

The theoretically predicted 100% spin polarization at the Fermi energy, ε_F, of CrO_2 makes it a promising material for magnetoelectronic devices [1–3]. According to Jullière's model, the magnetoresistance (MR) of a ferromagnet/insulator/ferromagnet tunnel junction depends on the spin polarization of the electrode material used [4]. The MR increases with increasing spin polarization of the ferromagnetic electrode material. Also, injection of spins from ferromagnetic metals into semiconductors may be allowed only for highly polarized metallic electrodes [5]. Additionally, transition-metal oxides like CrO_2, high-temperature superconductors and colossal magnetoresistance lanthanum-based manganates have attracted a lot of theoretical interest due to the complex interplay between orbital, structural and electronic degrees of freedom. This has revived research on half-metallic ferromagnetic transition-metal oxides, especially CrO_2, in the past few years. Unfortunately, CrO_2 is metastable at room temperature and atmospheric conditions and typically a thin Cr_2O_3 layer covers the CrO_2 surface. Methods like photoemission (PES), X-ray absorption (XAS) or X-ray magnetic circular dichroism (XMCD) spectroscopy could not easily be used for examination of basic properties of CrO_2, because of their intrinsic surface sensitivity. Therefore, only a few experimental results on single crystals or epitaxial-grown thin films have been published. Nevertheless, spectroscopic methods are able to give quantitative information about intrinsic magnetic properties of CrO_2.

✉ Fax: +49-711/689-1912, E-mail: goering@mf.mpg.de

2 Experiment and results

CrO_2 crystallizes in a tetragonal rutile-type structure, where chromium atoms form a body-centered tetragonal unit cell. Cr sites are octahedrally surrounded by oxygen atoms. The apical axis of the oxygen octahedra is oriented along the [110]([110]) direction for the edge (body-centered) Cr ions. The lattice parameters are $a = b = 4.421$ Å and $c = 2.916$ Å [6, 7]. CrO_2 is a metastable Cr-oxide phase at room temperature, orders ferromagnetically at $T_C = 393$ K and degrades above 400 K at ambient atmospheric pressures into the thermodynamically stable Cr_2O_3 phase. The CrO_2 film has been prepared by a chemical vapor deposition (CVD) technique proposed by Ishibashi et al. [8]. Al_2O_3 (0001) substrates have been used, which were annealed at 1000 °C for several hours before deposition. During the deposition, the substrate was oriented at an angle of 30° relative to the horizontal axis of the tube furnace. CrO_3 decomposes at a temperature of 260 °C within a two-zone tube furnace. A well-controlled flow of oxygen and a stabilized substrate temperature of 390 °C lead to approximately 200-nm-thick CrO_2 films. Characterization by X-ray diffractometry showed only CrO_2 (020) and (040) reflexes, indicating a preferred *a*-axis growth. Electron-diffraction analysis exhibits an artificial six-fold in-plane symmetry and a formation of twin boundaries [9]. A scanning electron microscopy (SEM) image of (010)-oriented CrO_2 crystallites on the Cr_2O_3 (0001) initial layer is shown in Fig. 1. The six-fold in-plane symmetry of the (0001)-oriented Cr_2O_3 initial layer (which is isostructural to Al_2O_3) leads to three equivalent in-plane orientations for the (011) plane of the CrO_2 unit cell. Transmission electron microscopy (TEM) analysis shows a small amount of Cr_2O_3 columns within the CrO_2 layer. More details of sample growth, characterization and magnetotransport properties have been published elsewhere [10]. The sam-

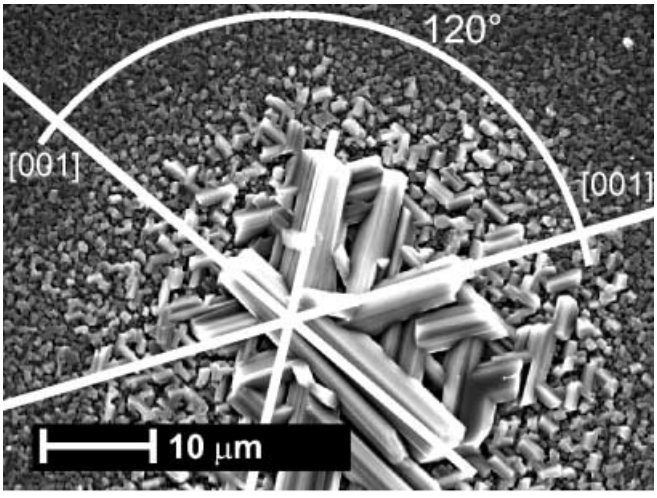

FIGURE 1 Scanning electron microscopy image of (010)-oriented CrO_2 crystallites on a Cr_2O_3 (0001) initial layer [10]

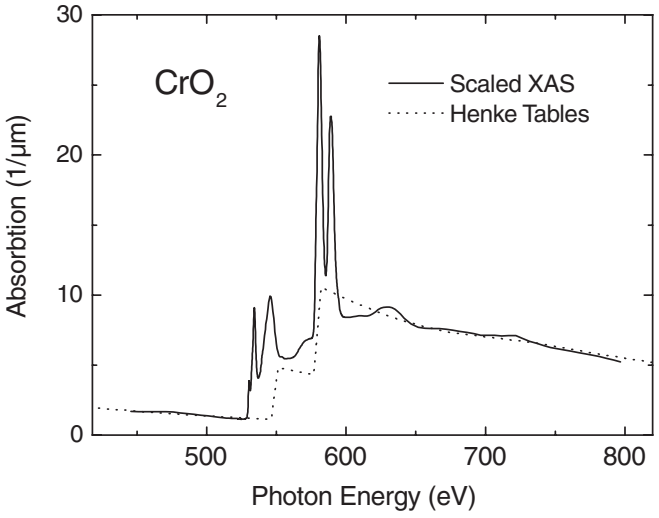

FIGURE 2 XAS spectra scaled to absolute CrO_2 absorption values averaged for parallel and antiparallel alignments of the photon $\boldsymbol{k}$-vector and the sample magnetization for normal incidence (*full line*) compared to CrO_2 adapted Henke table [11] values (*dotted line*)

ple has been exposed to air. No further treatment has been performed.

X-ray absorption spectra were recorded at the bending magnet beamline SX 700 III at BESSY I. The monochromator energy resolution was set to $E/\Delta E \approx 1200$ and the degree of circular polarization was 0.69 ± 0.05. Two Keithley 6517A electrometers were used for simultaneous measurement of the total drain sample current and the I_0 current from an Au-coated Cu grid. The I_0 grid was positioned in a μ-metal cylinder in order to prevent deviations produced by magnetic fields. A split-coil superconducting magnet system was used with a center bore of 5 cm and a maximum magnetic field of 30 kOe. All spectra have been recorded at magnetic fields of ± 5 kOe. The XMCD signal was carefully checked for self-absorption effects. Atomic absorption values of Cr and O have been extracted from tabulated values [11] and scaled to atomic densities in CrO_2. We shifted and scaled our measured XAS spectra for both magnetization directions to fit the pre-edge region of oxygen and the post-edge region of Cr $L_{2,3}$ edges of the calculated tabulated values. Due to this procedure, the resonant behavior of the absorption in the near-edge region could be estimated quantitatively. The resulting absorption coefficient is shown in Fig. 2. We extracted an absolute absorption length for the maximal absorption of 35 nm, which is significantly larger than the expected effective mean free path length of about 1.5 nm [12, 13]. After that, we modified our magnetic XAS spectrum (parallel and antiparallel alignment of helicity and magnetization) with the above-derived absolute absorption, using equation 5 and 7 from [13]. We compared observed small changes in the XAS spectra from normal to 60° incidence with simulated self-absorption-induced changes and could obtain the best agreement with our XAS data for an effective electron mean free path of only 0.7 nm. We applied sum rules to the original and self-absorption-modified spectra and compared orbital and spin contributions. Absolute changes between normal and 60° incidence are for the spin moment of $-0.005\mu_B$ ($-0.009\mu_B$) and for the orbital moment of $-0.0004\mu_B$ ($-0.0008\mu_B$) using an effective electron mean free path [12, 13] of 0.7 nm (1.5 nm). In comparison to the results of Nakajima et al. [13], self-absorption effects are not as strong as expected for a $3d^2$ system. Two different reasons are responsible for this reduction. CrO_2 has hybridization-related broadened L_2 and L_3 white lines, and therefore a strongly reduced maximal absorption compared to a pure metal spectrum with the same number of $3d$ holes. On the other hand, the chromium density and the Cr-related absorption coefficient are strongly reduced by dilution. Due to the nonlinear behavior, self-absorption is magnetically more effective for large differences between parallel and antiparallel orientations of sample magnetization and photon helicity, which is present in Fe or Co spectra but not in our CrO_2 spectra.

To prevent XMCD offset signals, we applied a small asymmetry of about 0.2 kOe in the external magnetic field, which does not influence the total sample magnetization [14]. To get a derivative-free XMCD signal the external magnetic field was flipped at each energy position. All shown XAS and XMCD spectra have been divided by the I_0 current, background-subtracted and edge-normalized. For parallel and antiparallel field alignments we used exactly the same background and the same normalization factor; therefore the shape of the dichroism spectrum is not affected. The photon beam was parallel aligned to the magnetic field. We show X-ray-absorption data for normal incidence $\Phi = 0°$ and more grazing incidence $\Phi = 60°$ (the geometry of the experimental setup is shown in Fig. 3).

The upper part of Fig. 4 shows the Cr $L_{2,3}$ normal-incidence absorption spectra of CrO_2 for parallel and antiparallel alignments of the photon k-vector and the applied magnetic field. In the lower part of Fig. 4 the corresponding XMCD signal for normal and grazing (60°) incidence is shown. An unusually clear and pronounced change in the spectral shape of the XMCD signal is clearly observable.

For a quantitative analysis, we calculated the projected orbital moments for the two given angles of incidence using sum rules [15, 16]. With a number of core holes $n_h = 8$ ($3d^2$ configuration) we extract raw values of projected orbital moments for normal incidence $L_z(0°) = -0.041\mu_B$ and for more grazing incidence L_z (60°) $= -0.016\mu_B$. Unfortunately, we

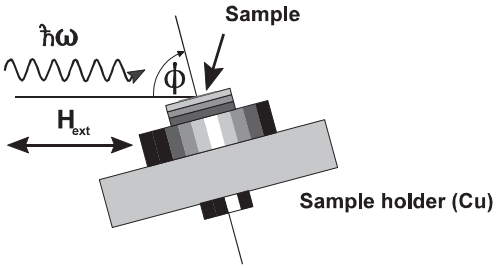

FIGURE 3 Schematic image of the experimental geometry

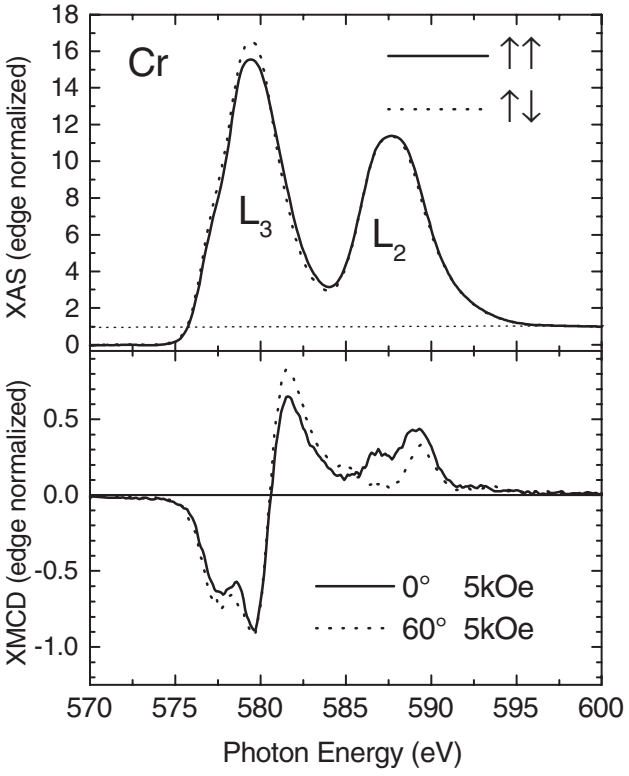

FIGURE 4 Normalized Cr $L_{2,3}$ absorption signal for parallel and antiparallel alignments of the photon $\boldsymbol{k}$-vector and the sample magnetization for normal incidence (*upper part*). *Lower part* shows the XMCD signal for normal (0°: *solid line*) and grazing (60°: *dotted line*) incidence

could not achieve technical saturation in 5-kOe external fields for the case of normal incidence due to the shape anisotropy of the sample. From detailed SQUID M(T, H) measurements (not shown), we correct for $T = 0$ K saturation magnetization and obtain for 0° (60°) a correction factor of 1.78 (1.41). The 0° value is slightly enhanced, due to the described shape-anisotropy correction. The 60° correction factor of 1.41 is related only to the temperature dependence, which is also the dominating part in the perpendicular-to-plane measurement. For thick samples, closure domains could be present at the sample surface and differences between surface-related XMCD TEY (Total Electron Yield)-projected magnetizations and SQUID-derived values could appear. This is not the case in our measurement. In Fig. 5 we show in-plane and out-of-plane SQUID M(H) curves and XMCD L_3-edge-related out-of-plane hysteresis loops. The SQUID and XMCD curves are in perfect agreement and therefore our above-described SQUID-derived normal-incidence absolute correction factor

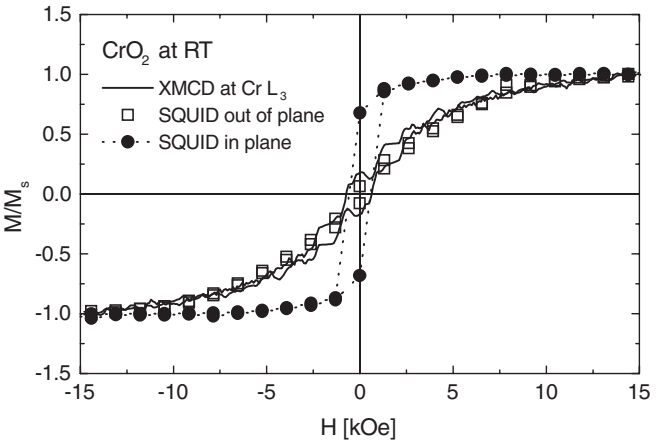

FIGURE 5 XMCD L_3-edge-related out-of-plane hysteresis loop (*straight line*) compared to SQUID-derived out-of-plane (*hollow rectangles*) and in-plane (*filled circles*) curves

of 1.71 is not disturbed by this possible TEY-related artefact. The technique used to obtain high-quality TEY-related XMCD hysteresis loops has been described in detail elsewhere [17]. By further correcting for the degree of circular polarization, we can obtain $L_z(0°) = -0.105\mu_B$ and $L_z(60°) = -0.034\mu_B$.

3 Moment analysis

3.1 *Introduction to moment analysis for 3d transition metals*

We analyze the $L_{2,3}$ dichroism spectra in terms of ground-state moments [18, 19]. The advantage of this method is the possibility to get quantitative values even for the light transition-metal (TM) ions with a small p-shell spin–orbit coupling (SOC). In principle, moment analysis tries to gain information from the shape of the XMCD spectrum. This is an advantage compared to sum-rule analysis, which only uses integral values for the L_2 and L_3 parts of the XMCD spectrum separately. Therefore sum rules could not give reasonable values for the projected spin moments if L_2 and L_3 XMCD features overlap in energy. Another advantage of this moment analysis is the possibility to gain quantitative information about spin and other ground-state moments, which have contributions to the observed XMCD signal like the number of core holes and the spin–orbit term. While this method is related to an atomic picture, which takes into account the coupling of the core hole to the final-state d shell, band-structure effects could be considered by Lorentzian or Gaussian broadening and by the use of different energy levels. This could yield, for example, to magnetization values for spectrally resolved and well-separated sublevels, like t_{2g} or e_g contributions in many TM oxides. This has been demonstrated for the ferrimagnetic iron garnets, where octahedrally and tetrahedrally coordinated Fe^{3+} ions could be identified separately by XMCD [20, 21]. We believe that the Cr $L_2 - L_3$ edge separation is strong enough to apply moment analysis. Experimental results for Cr metal from O'Brien et al. [22] clearly show that XMCD features from the L_3 and L_2 edges are separated. The results of van der Laan [18, 19] and the results of O'Brien et al. show exactly the same behavior. So,

the present broadening in the CrO_2 $L_{2,3}$ spectra compared to the pure metal spectra is related to hybridization effects. It is clear that, in a covalent type of bonding, different electron configurations could be present (for example d^1, d^2 or d^3), which could yield to correlation effects. These results in multiplet-like features, which are considered by a configuration interaction (CI) ligand-field multiplet calculation. Early calculations of de Groot et al. [23] have shown that the cubic crystal field is very strong. Recent results of van Elp and Tanaka [24] clearly mention the dominating part of the crystal symmetry and the strength of oxygen hybridization to O K-edge spectral features of some TM oxides. From this point of view, crystal-field effects are strong and the resulting energies of the CI calculations nearly represent band-structure center-of-gravity positions. The below-described quite good agreement between experiment and fit, the direct correspondence to the band-structure-related projected density of states (DOS) and the reduced number of free fitting parameters give strong support that the moment analysis is a good representation of the XMCD spectra that leads to well-separated L_2 and L_3 spectral features.

3.2 *Application to* CrO_2

It has been verified that oxygen K-edge spectra represent the $2p$ hybridized part of the band structure and give an image of the unoccupied projected O $2p$ DOS [25]. Influences of the core hole could be considered by a configuration-interaction scheme [24]. Due to this projection behavior, the main features could be understood by quantitative comparison to recent band-structure calculations [1–3, 26]. O K spectra and band-structure calculations could give similar information. We have separated O K-edge spectra of CrO_2 into two different regions. First, 1 eV above threshold, which is unambiguously identified as unoccupied t_{2g} majority states and, second, a broader feature around 3 eV above, which corresponds to a mixture of t_{2g} e_g minority and the e_g majority states [27]. The latter represents band-structure-related values [1–3, 26]. This energy separation is also present in CrO_2 $L_{2,3}$ spectra, which have a more complicated shape compared to simple pure and metallic TM spectra. The total width of the broader structure is about 7 eV [1], but the dominating part has a FWHM of only 3 eV. Considering the given arguments, we try to interpret the $L_{2,3}$ XAS and XMCD spectra by the use of only two different energies for the moment analysis, which are separated by 2.9 eV, and only Lorentzian line broadening has been applied. For a reduction of free fitting parameters, the energy position, line width, effective $2p3d$ exchange and the $2p$ SOC energy (see Table 1) are previously estimated and have been held fixed. Also, the sum of the projected orbital moments was constrained to the above-discussed sum-rule values. All fixed parameters are shown in Table 1. The FWHM values have been chosen to fit the XMCD data and to match roughly band-structure-related values. The value for the $2p$ SOC energy has been taken from [28, 29].

For the moment-fitting procedure the relative energy-dependent ratios for the atomic-like different sublevels have been taken from [18, 19]. For data fitting we used the w^{000}, w^{011}, w^{101} and w^{110} moments, which are proportional to the number of holes in the d shell (n_h), the spin moment S_z, the orbital moment L_z and to $\boldsymbol{L} \cdot \boldsymbol{S}$, respectively. The areas corresponding to the w^{011} and w^{101} moments have been used for sum-rule analysis. In Table 2 we show the fitted moment

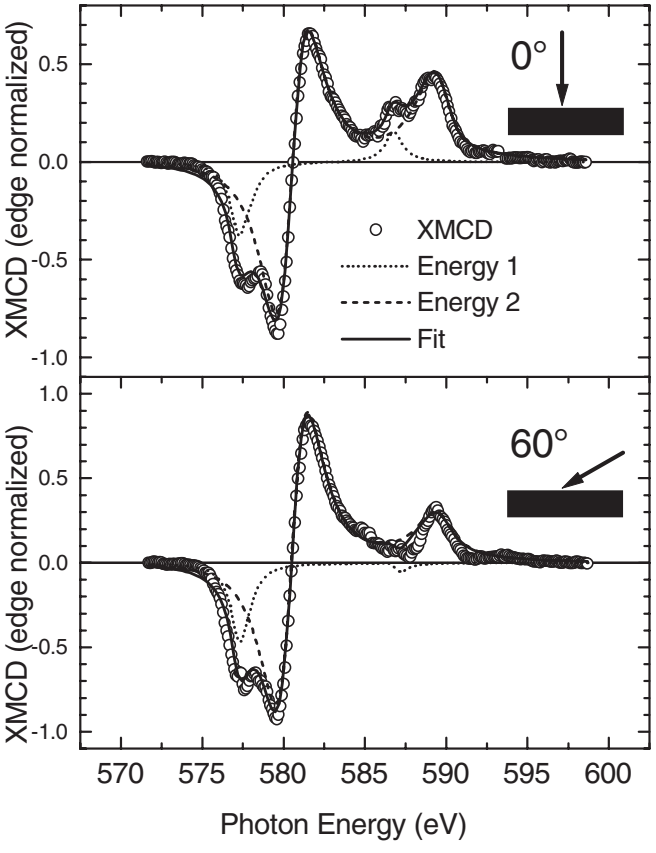

FIGURE 6 Moment-analysis fit results for normal (*above*) and grazing (*below*) incidence (*circle*: measurement; *dotted*: fit at energy 577.6 eV; *dashed*: fit at energy 580.5 eV; *solid line*: fitted sum)

Energy 1	FWHM 1	Energy 2	FWHM 2	$2p$ SOC	Eff. $2p3d$ exch.
577.6 eV	1.3 eV	580.5 eV	3.3 eV	9.3 eV	0.45 eV

TABLE 1 Fixed-fit parameters for moment analysis

	$E_0 = 577.6$ eV			$E_1 = 580.5$ eV					
Angle	w^{000} $\propto n_h$	w^{011} $\propto S_z$	w^{101} $\propto L_z$	w^{000} $\propto n_h$	w^{011} $\propto S_z$	w^{101} $\propto L_z$	w^{110} $\propto L^*S$	$S_{z0}+S_{z1}$	$L_{z0}+L_{z1}$
	(arb. units)	(μ_B)	(μ_B)	(arb. units)	(μ_B)	(μ_B)	(arb. units)	(μ_B)	(μ_B)
0°	1.03	0.25	0.05	49.8	0.73	–0.15	3.3	0.98	–0.1
60°	1.29	0.12	0.11	44.8	0.34	–0.14	21.9	0.46	–0.03

TABLE 2 Moment-analysis fit results

data, while spin and orbital moments have been corrected for $T = 0$ K saturation.

In Fig. 6 we show fit results of our moment analysis for each energy and the sum of both for 0° and 60° angles of incidence, which represent our XMCD spectra nearly perfectly. All structures and tendencies could be reproduced by this simple two-energy fit.

Four fit parameters change significantly with rotation: the spin and the orbital contribution of the lower energy, and the spin and the SOC (Spin-Orbit-Interaction) contribution of the higher-energy part in the XMCD spectrum.

4 Discussion

4.1 *Spin anisotropy and magnetic dipole term T_z*

First, we want to discuss the projected spin moments. For both energies the observed projected spin moments change by a factor of two and the sum decreases from approximately $1.0\mu_B$ to $0.5\mu_B$ (see Table 2). This is quite unusual compared to XMCD-related spin values of other transition metals, where only very small changes have been observed for saturated samples. To obtain the moment-analysis spin values, we simply used conventional sum rules by artificially separating the L_3 from the L_2 edge at a splitting energy of 584.9 eV. The unknown offshoot from the L_3 edge is present at the L_2 XMCD area and therefore is missing at the L_3 edge. Compared to moment-analysis-derived spin values, this results in an increase of 10% for the spin moment, but the trends and the general reduction by a factor of two are similar to moment-analysis-derived values. As discussed above, we could not perfectly saturate the sample along the normal direction. This simply should result in a reduced spin moment but not in a strong increase by a factor of two.

This angle-dependent change suggests a very strong magnetic dipole term T_z, which is directly related to a quadrupolar spin distribution, originated by a reduced symmetry that is less than cubic. For the case of strong symmetry breaking, given at an interface, where the octahedral surface symmetry is broken by the adjacent constituent, T_z could be significantly increased. Calculations have shown that for a $3d^2$ configuration this surface-induced symmetry breaking gives a T_z of about 20% of the spin moment [30]. In the case of CrO_2 the local octahedral environment is distorted in the rutile structure; therefore the T_z (index z is related to a local distortion) value could be significantly enhanced. Estimating now the spin moment, the $3d$ symmetry relation $\langle T_z\rangle_x + \langle T_z\rangle_y + \langle T_z\rangle_z = 0$ has been applied, which has been published by Stöhr and König [31] and verified on a Au/Co/Au wedge by Weller et al. [32]. Transferring this equation to the rutile-type unit cell yields $2\langle T_z\rangle_a + \langle T_z\rangle_c = 0$. Measuring along the a axis (0°), only $\langle T_z\rangle_a$-axis contributions are present due to the film's texture, while more grazing incidence gives rise to a more complicated mixture of a- and c-axis magnetic dipole term contributions. For 60° grazing incidence and a random in-plane c- (a-) axis distribution, there is an in-plane mixture of a and c axes and an effective $\langle T_z\rangle$ projection of $\sin(60°)(\langle T_z\rangle_a + \langle T_z\rangle_c)2/\pi$, while the off-plane contribution is simply $\cos(60°)\langle T_z\rangle_a$. To estimate the zero-$\langle T_z\rangle$ condition we have to calculate $S_z(60°) + S_z(0°)(\sin(60°)2/\pi - \cos(60°))$, which cancels out $\langle T_z\rangle$ contributions and normalizes by $(1 + \sin(60°)2/\pi - \cos(60°))$. This results in a corrected spin moment without any magnetic dipole term contribution of $S_{\text{zeff}} = 0.49\mu_B$. For a fully spin-polarized system with an empty minority band a d^2 configuration yields a spin moment of $2\mu_B$, which has been experimentally and theoretically verified. SQUID measurements performed on the sample used exhibit the same value. A correct treatment of the 120° c-axis in-plane distribution instead of the random model used above leads to a spin moment from 0.46 to $0.50\mu_B$, depending on the unknown in-plane orientation of the sample relative to the photon beam.

The extracted effective XMCD spin moment of $0.49\mu_B$ is about a factor of 4.1 too small compared to SQUID data, which is a rather large deviation.

In this section some possible explanations for this strong reduction will be discussed.

Due to the small spin–orbit splitting for light $3d$ transition metals, there are two dominating problems. Firstly, spectral features of the L_2 and the L_3 edges are overlapping and therefore sum rules could give wrong values. Due to the moment analysis, we could avoid this problem. Secondly, the final states could not be considered as pure L_2 or L_3 states because of quantum-mechanical mixing. Therefore, the spectral intensity in the L_3 region has L_2 contributions and vice versa. This has been calculated for the case of Cr^{2+} ($3d^4$), where a reduction of about 50% has been proposed [30], but this strong reduction has been obtained by sum-rule application to theoretical XMCD spectra. Following the spectral simulation in this reference, it is not clear whether the dominant part of the reduction is related to overlapping features, discussed above, or to real L_2–L_3 final-state mixing. Assuming such a mixing present in CrO_2, we have a Cr d^2 configuration with the same $L_{2,3}$-edge spin–orbit splitting, and the theoretically proposed effect could be a suitable explanation of this strong reduction in the observed spin moment.

A third point is related to the spin–orbit coupling in the $3d$ shell. If a spin and an orbital moment are present, the octahedral symmetry could be reduced by SOC itself and a nonvanishing T_z is present. This has also been calculated by Crocombette et al. [30]. If the SOC is isotropic, the T_z moment is always oriented along the spin moment and varies with the sample magnetization. The sample orientation will not change this spin-induced T_z; therefore the above-used symmetry relation $\langle T_z\rangle_x + \langle T_z\rangle_y + \langle T_z\rangle_z = 0$ is no longer valid and T_z is always present. Reported calculations for a $3d^2$ configuration have shown that SOC itself could give a T_z contribution up to 13% of the spin moment, but only at zero temperature. For room-temperature measurements this SOC-induced value is strongly decreased to about 1% relative to the spin part. Our experiments have been performed at room temperature; therefore we conclude that this SOC-induced T_z is not the origin of the observed reduction of the spin moment, despite the possibility that for CrO_2 the SOC could be strongly enhanced.

A fourth and probably most interesting point for the effective XMCD spin-moment reduction is related to hybridization. Due to hybridization, the wave functions of the $3d$ electrons are partly delocalized and form a mixture of Cr $3d$- and O $2p$-like states. Therefore, parts of the electronic wave function will not overlap any more with $2p$ initial-state wave functions. This would induce a decrease in the XMCD ef-

fect for high-bandwidth metals like Fe or Co, corresponding to the strongly delocalized behavior of the 3*d* electrons, which has not been observed. In fact, for pure Fe and Co, nearly perfect agreement could be achieved between sum-rule-related magnetic moments and other experimental and theoretical values [33]. But, the mixing or hybridization of the 3*d* electrons in a pure metal happens between Fe–Fe nearest neighbors and, therefore, the electrons are bisected between different Fe ions. On average, all 3*d* electrons are located only on Fe sites. The 3*d* band-like electron wave functions are of dominating Fe 3*d* character and no reduction of the magnetic moment has been observed [33]. This argument is supported by XMCD measurements performed on rare-earth iron garnets ($Re_3Fe_5O_{12}$ or ReIG; Re: rare earth). For HoIG [20], DyIG [21] and GdIG [34, 35], the Fe $L_{2,3}$ XMCD has been studied for different temperatures and sum rules have been applied at the Fe $L_{2,3}$ edges. In contrast to the Fe metal XMCD data of Chen et al. [44], a reduction of the spin moment by a factor of two for the Fe $L_{2,3}$ XMCD has been observed [20, 21]. For the pure Fe system nearly no reduction of the magnetic moment due to overlapping $L_{2,3}$ features or $L_{2,3}$ final-state mixing is present [15, 30]; therefore, the reduction of the magnetic moment present in the garnets could not be related to this issue. We have also performed XMCD measurements and moment analysis, as described above, at the Mn $L_{2,3}$ edges of $La_{1-x}Ca_xMnO_3$, and again a reduction of the spin moment by a factor of two has been observed [36, 37]. XMCD of 'ferromagnetic' Cr could be used in principle for comparison, but the Cr ground state is antiferromagnetic. To achieve ferromagnetically ordered Cr, it has to be deposited on or diluted in a ferromagnet [22, 38–40]. For Co and Fe substrates, Cr is ordered antiferromagnetically with respect to the ferromagnetic substrate. The absolute moment used for normalization of the XMCD spectra is still questionable, because the magnetic moment of the reference system, a FeCr alloy with low Cr concentration, is not well defined [41]. In this reference system Cr is dominantly hybridized with Fe ions and the influence of hybridization on the Cr XMCD is not known.

To summarize the discussion of the spin moment, we believe that hybridization with oxygen plays a dominant role and the observed reduction in the magnetic spin moment in combination with bulk magnetization data and theoretical calculations could be used to investigate hybridization and oxygen coupling. Residual Cr_2O_3 spectral weight, further discussed below, reduces the XMCD spin moment as well as $L_{2,3}$ mixing with an unknown reduction strength. Further investigations of epitaxially grown CrO_2 thin films on TiO_2 substrates with a probably lower Cr_2O_3 contribution could give more insight for quantitative estimation of the magnetic dipole term T_z.

A further argument for XMCD spin reduction is related to Cr_2O_3 spectral contributions, which will be discussed below.

4.2 *Orbital anisotropy*

In this section the observed changes of the orbital moment will be discussed.

Using conventional sum-rule analysis, we find negative orbital moments for pure *a*-axis projections and for increased *c*-axis contributions (see above or Table 2), which is consistent with Hund's-rule coupling for a less than half-filled 3*d* band. From a simple sum-rule analysis, we get a decreased absolute projected orbital moment along the magnetic easy *c*-axis and a higher one along the hard *a*-axis, which is quite unexpected, because the easy axis for a nearly unstrained thin film is the *c*-axis [27, 42]. This is in contradiction to Bruno's model for the intrinsic origin of magnetocrystalline easy-axis behavior with increased and nondecreased absolute orbital projections along the easy axis [43, 44]. Focusing on the lower part of Fig. 4, we can visually identify spectral changes present at 577.6 eV and 586.9 eV, which are separated by 9.3 eV (related to $2p$ SOC). This behavior suggests a dominant change in the projected orbital moment and is reflected by the moment-analysis fit in Table 2, where only the narrow-band unoccupied majority t_{2g} feature at 577.6 eV shows significant changes in the orbital contribution of $0.06\mu_B$. In contrast, the broad-band feature at 580.5 eV has a nearly constant orbital moment. This result is quite important, because it confirms Bruno's model. A positive orbital moment is strongly increased along the easy *c*-axis while a constant negative orbital background, corresponding to a broad majority e_g and minority t_{2g} e_g mixture, is present. Bruno pointed out that quenching of the orbital moment is related to the ratio of the 3*d* effective SOC constant ξ to the effective bandwidth W. For the unoccupied majority t_{2g} feature at 577.6 eV, the fitted effective bandwidth is only $W = 1.3$ eV and a corresponding large residual orbital moment is present, while the broad-band feature at 580.5 eV has a higher bandwidth of $W = 3.3$ eV and, therefore, a smaller orbital contribution.

The orbital moment is not influenced by $L_{2,3}$ mixing and overlapping problems, because both edges have the same sign and a mixing will not reduce the XMCD-related projected orbital moment.

Due to the strong shape anisotropy, we were unable to identify unambiguously the magnetic easy axis of the sample. We fitted our hysteresis SQUID data with a Stoner–Wohlfart model, which suggests an intrinsic easy axis along the *c*-axis.

Summarizing the discussion of the orbital moment, large changes in the orbital contribution by increased *c*-axis projections have been identified. Using the technique of moment analysis, we identified those changes with an unoccupied majority t_{2g} feature at 577.6 eV, while the higher-energy mixed states provide a nearly constant orbital background with a negative sign.

4.3 Cr_2O_3 *contributions*

For a quantitative estimation of the Cr_2O_3 spectral weight in our measurements we measured O *K*-edge spectra and fitted the normalized XAS data to digitized reference spectra for CrO_2 and Cr_2O_3 [27]. This reference data has been slightly broadened to fit our experimental conditions. Afterwards, a simulated CrO_2 normal-incidence and 60° spectrum was synthesized by a weighted-average sum of pure *a*- and *c*-axes spectra. Figure 7 shows O *K*-edge XAS for normal incidence and the fit result. CrO_2 and Cr_2O_3 contributions are also shown and an effective O *K*-edge spectral weight ratio of $CrO_2/Cr_2O_3 = 1.3 \pm 0.2$ has been extracted. Due to this contamination, a Cr_2O_3-related nonmagnetic resonant part in the

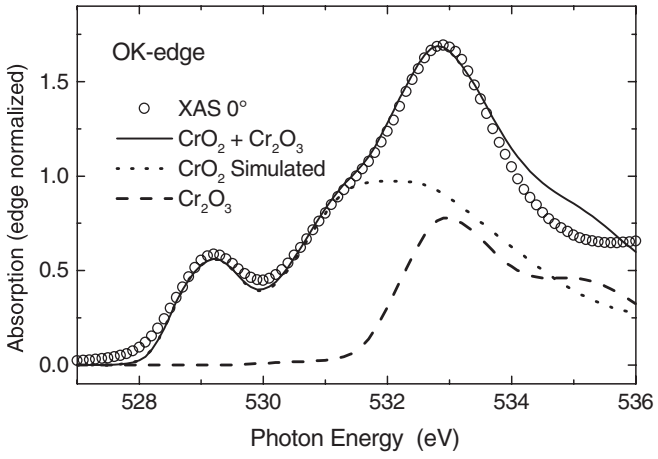

FIGURE 7 Normal-incidence oxygen *K*-edge XAS spectrum (*open circles*); CrO_2 simulated for circularly polarized light [27] with equal *a*- and *c*-axis contributions (*dotted*), Cr_2O_3 (*dashed*) and the weighted fit results (*solid*)

Cr $L_{2,3}$ XAS spectrum (Fig. 4, upper part) is present, which is not related to CrO_2. Therefore, the resonant XAS intensity used by the sum-rule analysis is overestimated and the Cr 3*d* magnetic moments are underestimated. Assuming that this ratio stays constant for O *K* and Cr $L_{2,3}$ edges, we could estimate the nonmagnetic Cr_2O_3-related spectral weight in the nonmagnetic XAS resonance lines and calculate a correction factor of $1 + (1/1.3) = 1.8(-0.2/+0.3)$ for all magnetic moments, which have been extracted by sum-rule or moment analysis. The error bar has been calculated by quantitative estimation of the maximal Cr_2O_3 contamination spectral weight in the CrO_2 reference spectra [27], which leads to an underestimation of Cr_2O_3. Using intensity relations from Nakajima et al. [13] and an effective mean free path of 1.5 nm, we could obtain a maximal Cr_2O_3 thickness of 0.4 nm, which is 0.6-nm smaller than the original tunneling-derived thickness value.

With this correction the effective absolute averaged projected Cr *d* spin moment will be $0.9 \pm 0.2\mu_B$ and the total change in the orbital moment is $0.12\mu_B$.

5 Conclusions

We identified the intrinsic magnetic easy axis of CrO_2, which is oriented along the rutile *c*-axis, by an increase in orbital contributions for unoccupied majority t_{2g} electrons. This result could only be obtained by the use of an XMCD analysis in terms of ground-state moments and demonstrates the possibility to derive much more quantitative information from XMCD measurements, even without further theoretical support. Sum-rule-related spin values could be obtained, which take into account spectral overlap in light TM oxides. An unusually large T_z term has been found.

ACKNOWLEDGEMENTS We would like to thank T. Kachel and H. Gundlach for kind user support at BESSY, and S. Gold, A. Bayer, F. Weigand and A. Peter for helpful discussions. This work was performed at and supported by BESSY. Additional financial support was by BMBF (05SC8WW1) and DFG (Schu 964/2-3).

REFERENCES

1 M.A. Korotin, V.I. Anisimov, D.I. Khomskii, G.A. Sawatzky: Phys. Rev. Lett. **80**, 4305 (1998)
2 S.P. Lewis, P.B. Allen, T. Sasaki: Phys. Rev. B **55**, 10 253 (1997)
3 K. Schwarz: J. Phys. F: Met. Phys. **16**, L211 (1986)
4 M. Jullière: Phys. Lett. **54A**, 225 (1975)
5 G. Schmidt, D. Ferrand, L.W. Molenkamp, A.T. Filip, B.J. van Wees: Phys. Rev. B **62**, R4790 (2000)
6 P. Porta, M. Marezio, J.P. Reimeika, P.D. Dernier: Mater. Res. Bull. **7**, 157 (1972)
7 B.J. Thamer, R.M. Douglass, E. Staritzky: J. Am. Chem. Soc. **79**, 547 (1957)
8 S. Ishibashi, T. Namikawa, M. Satou: Mater. Res. Bull. **14**, 51 (1979)
9 M. Rabe, J. Pommer, K. Samm, B. Özyilmas, C. König, M. Fraune, U. Rüdiger, G. Güntherodt, S. Senz, D. Hesse: J. Phys.: Condens. Matter **14**, 7 (2002)
10 U. Rüdiger, M. Rabe, K. Samm, B. Özyilmas, J. Pommer, M. Fraune, G. Güntherodt, S. Senz, D. Hesse: J. Appl. Phys. **89**, 7699 (2001)
11 B.L. Henke, E.M. Gullikson, J.C. Davis: At. Data Nucl. Data Tab. **54**, 181 (1993)
12 V. Chakarian, Y.U. Idzerda: J. Appl. Phys. **81**, 4709 (1997)
13 R. Nakajima, J. Stöhr, Y.U. Idzerda: Phys. Rev. B **59**, 6421 (1999)
14 E. Goering, S. Gold, A. Bayer, G. Schuetz: J. Synchrotron Radiat. **8**, 434 (2001)
15 P. Carra, B.T. Thole, M. Altarelli, X. Wang: Phys. Rev. Lett. **70**, 694 (1993)
16 B.T. Thole, P. Carra, F. Sette, G. van der Laan: Phys. Rev. Lett. **68**, 1943 (1992)
17 E. Goering, A. Fuss, W. Weber, J. Will, G. Schuetz: J. Appl. Phys. **88**, 5920 (2000)
18 G. van der Laan: Phys. Rev. B **55**, 8086 (1997)
19 G. van der Laan: J. Phys.: Condens. Matter **9**, L259 (1997)
20 E. Goering, S. Gold, G. Schuetz: J. Synchrotron Radiat. **8**, 422 (2001)
21 S. Gold, E. Goering, A. Bayer, G. Schuetz: (2001) in preparation
22 W.L. O'Brien, B.P. Tonner, G.R. Harp, S.S.P. Parkin: J. Appl. Phys. **76**, 6462 (1994)
23 F.M.F. de Groot, J.C. Fuggle, B.T. Thole, G.A. Sawatzky: Phys. Rev. B **42**, 5459 (1990)
24 J. van Elp, A. Tanaka: Phys. Rev. B **60**, 5331 (1999)
25 E. Goering, O. Müller, M. Klemm, M.L. den Boer, S. Horn: Philos. Mag. B **75**, 229 (1997)
26 D.I. Khomskii, G.A. Sawatzky: Solid State Commun. **102**, 87 (1997)
27 C.B. Stagarescu, X. Su, D.E. Eastman, K.N. Altmann, F.J. Himpsel, A. Gupta: Phys. Rev. B **61**, R9233 (2000)
28 J.A. Bearden, A.F. Burr: Rev. Mod. Phys. **39**, 125 (1967)
29 J.C. Fuggle, N. Martensson: J. Electron. Spectrosc. Relat. Phenom. **21**, 275 (1980)
30 J.P. Crocombette, B.T. Thole, F. Jollet: J. Phys.: Condens. Matter **8**, 4095 (1996)
31 J. Stöhr, H. König: Phys. Rev. Lett. **75**, 3748 (1995)
32 D. Weller, J. Stöhr, R. Nakajima, A. Carl, M.G. Samant, C. Chappert, R. Megy, P. Beauvillain, P. Veillet, G.A. Held: Phys. Rev. Lett. **75**, 3752 (1995)
33 C.T. Chen, Y.U. Idzerda, H.J. Lin, N.V. Smith, G. Meigs, E. Chaban, G.H. Ho, E. Pellegrin, F. Sette: Phys. Rev. Lett. **75**, 152 (1995)
34 P. Rudolf, F. Sette, L.H. Tjeng, G. Meigs, C.T. Chen: J. Appl. Phys. **70**, 6338 (1991)
35 P. Rudolf, F. Sette, L.H. Tjeng, G. Meigs, C.T. Chen: J. Magn. Magn. Mater. **109**, 109 (1992)
36 E. Goering, J. Will, G. Schuetz: (2001) in preparation
37 J. Will: Diploma Thesis, Würzburg (1999)
38 Y.U. Idzerda, L.H. Tjeng, H.J. Lin, C.J. Gutierrez, G. Meigs, C.T. Chen: Phys. Rev. B **48**, 4144 (1993)
39 K.M. Kemner, Y.U. Idzerda, V.G. Harris, V. Chakarian, W.T. Elam, C.-C. Kao, E. Johnson, Y.C. Feng, D.E. Laughlin, C.T. Chen, K.-B. Lee, J.C. Lodder: J. Appl. Phys. **81**, 1002 (1997)
40 M.A. Tomaz, W.J. Antel, Jr., W.L. O'Brien, G.R. Harp: Phys. Rev. B **55**, 3716 (1997)
41 M.B. Stearns, L.A. Feldkamp: Phys. Rev. B **13**, 1198 (1976)
42 X.W. Li, A. Gupta, G. Xiao: Appl. Phys. Lett. **75**, 713 (1999)
43 P. Bruno, J. Seiden: J. Phys. Colloq. **49**, 1645 (1989)
44 P. Bruno: Phys. Rev. B **39**, 865 (1989)